

Investigation on Microstructure and Impact Toughness of Different Zones in Duplex Stainless Steel Welding Joint

Zhiqiang Zhang, Hongyang Jing, Lianyong Xu, Yongdian Han, Guolu Li, and Lei Zhao

(Submitted January 22, 2016; in revised form October 31, 2016; published online November 22, 2016)

This paper investigated on microstructure and impact toughness of different zones in duplex stainless steel welding joint. High-temperature heat-affected zone (HTHAZ) contained coarse ferrite grains and secondary precipitates such as secondary austenite, Cr_2N , and sigma. Intergranular secondary austenite was prone to precipitation in low-temperature heat-affected zone (LTHAZ). Both in weld metal (WM) and in HTHAZ, the austenite consisted of different primary and secondary austenite. The ferrite grains in base metal (BM) presented typical rolling texture, while the austenite grains showed random orientation. Both in the HTHAZ and in the LTHAZ, the ferrite grains maintained same texture as the ferrite in the BM. The secondary austenite had higher Ni but lower Cr and Mo than the primary austenite. Furthermore, the WM exhibited the highest toughness because of sufficient ductile austenite and unapparent ferrite texture. The HTHAZ had the lowest toughness because of insufficient austenite formation in addition to brittle sigma and Cr_2N precipitation. The LTHAZ toughness was higher than the BM due to secondary austenite precipitation. In addition, the WM fracture was dominated by the dimple, while the cleavage was main fracture mode of the HTHAZ. Both BM and LTHAZ exhibited a mixed fracture mode of the dimple and quasi-cleavage.

Keywords duplex stainless steel, fracture, microstructure, toughness, welding

1. Introduction

Duplex stainless steel (DSS), with nearly equal proportion of ferrite (δ) and austenite (γ) phase, near-perfectly combines most of the beneficial properties of austenitic stainless steel (ASS) and ferritic stainless steel (FSS), including high strength, good toughness, and excellent corrosion resistance (Ref 1-3). Thus, DSS is increasingly being applied in various fields such as marine, power, chemical, transportation, desalination, paper, petroleum, and natural gas industries (Ref 4-7).

To attain excellent properties, DSS is recommended to maintain a δ/γ ratio close to 1:1 (Ref 8). However, this dual-phase balance in weld metal (WM) and heat-affected zone (HAZ) will be disturbed during welding process (Ref 9-11). It is well known that welding is an inevitable fabrication process in most of the applications of DSS. Gas tungsten arc welding (GTAW) is one of the most popular techniques for welding DSS because it produces high-quality welds to meet service requirements, although its low welding efficiency restricts its applications to some extent (Ref 12-14). After welding thermal

cycles, the materials in both the HAZ and the WM show some apparent changes in the microstructure including excessive ferritization and undesirable secondary precipitates [such as sigma (σ) and Cr_2N], as reported by Ramirez et al. (Ref 15-17). The excessive ferritization and undesirable precipitates can cause the deterioration of mechanical properties and corrosion resistance of DSS welding joint (Ref 1, 18, 19). Furthermore, when the DSS joint is reheated, as in the multi-pass welding, the most apparent changes in the microstructure are secondary austenite (γ_2) and Cr_2N precipitation (Ref 15, 17, 20, 21). The γ_2 precipitation can improve the toughness of DSS but compromises the corrosion resistance, while the Cr_2N precipitation usually reduces the toughness and corrosion resistance, as reported by Chahuan et al. (Ref 15, 17, 20, 22). However, the influence of the γ_2 and Cr_2N precipitation in the HAZ and the WM on mechanical properties and corrosion resistance is still relatively limited currently.

Although impact toughness is usually used as an important indicator for assessing the mechanical property of a material, there are only a few studies on toughness of different zones (including WM, HAZ, and BM) in the DSS welding joint. Generally, the impact toughness of the DSS welding joint markedly decreased with the increase in heat input because of the increase in ferrite content, as reported by Sathiya et al. (Ref 23). In addition, Ramkumar et al. (Ref 24) have studied the influence of different filler metals on the impact toughness of the DSS welding joint and revealed that the ER2553 weld exhibited greater impact toughness than the ERNiCrMo-4 weld. Jebaraj et al. (Ref 25) studied that the influence of post-weld heat treatment on the impact toughness of DSS BM (AISI 2205) and WM (ER2209) and revealed that solution treatment at 1050 °C caused noticeable improvement in toughness at -40 °C in the WM due to the increase in ductile austenite phases. But the impact energy significantly decreased in the

Zhiqiang Zhang, Hongyang Jing, Lianyong Xu, Yongdian Han, and Lei Zhao, School of Materials Science and Engineering, Tianjin University, Tianjin 300350, China; Tianjin Key Laboratory of Advanced Joining Technology, Tianjin 300350, China; and Guolu Li, School of Materials Science and Engineering, Hebei University of Technology, Tianjin 300130, China. Contact e-mail: xulianyong@tju.edu.cn.

BM after heat treatment at 1050 and 850 °C, which was due to ferrite grain growth and σ phase precipitation, respectively. In addition, Zhang et al. (Ref 17) studied the influence of microstructure evolution on the impact property of the DSS joint welded by using different methods and indicated that the HAZ had much lower impact toughness than the BM and the WM due to the coarse ferrite grain, the insufficient austenite content, and the Cr_2N precipitation. However, the influence of microstructural changes on the impact toughness of the different zones in the DSS welding joint, including the WM, BM, and different HAZs, has not been systematically studied yet.

The aim of this paper was to investigate the microstructure and impact toughness of the different zones in the DSS welding joint by using optical microscopy (OM), electron backscatter diffraction (EBSD), scanning electron microscopy (SEM), transmission electron microscopy (TEM), energy-dispersive spectroscopy (EDS), electron probe microanalysis (EPMA).

2. Experimental Procedure

2.1 Materials and Welding Procedure

A UNS S31803 DSS plate with 14 mm thickness was used as the BM in the present study, which had been hot-rolled followed by solution treatment at 1040-1100 °C for 1 h and then quenched in water. According to Welding Research Council (WRC) diagram (Ref 26), ER2209 with a diameter of 1.2 mm was used as the filler wire. The chemical compositions of the BM and the filler wire are listed in Table 1. As compared to the BM, the filler wire had higher Ni and Cu contents for facilitating austenite formation. In this study, the GTAW technique was used to prepare multi-pass DSS welding joint. The schematic of the welding process is shown in Fig. 1. Because the HAZ width was less than 2 mm, to obtain a straight edge HAZ for the exactly sampling impact specimen in the different HAZs, a single bevel with an angle of 45° was

Table 1 Chemical compositions of base metal and filler metal

Materials	Chemical compositions (wt.%)										
	C	Si	Mn	P	S	Ni	N	Cr	Mo	Cu	Fe
Base metal (UNS S31803)	0.018	0.54	0.92	0.011	0.003	5.3	0.17	22.9	3.0	0.042	Bal
Filler metal (ER2209)	0.008	0.48	1.54	0.017	0.0006	8.63	0.15	22.94	3.07	0.14	Bal

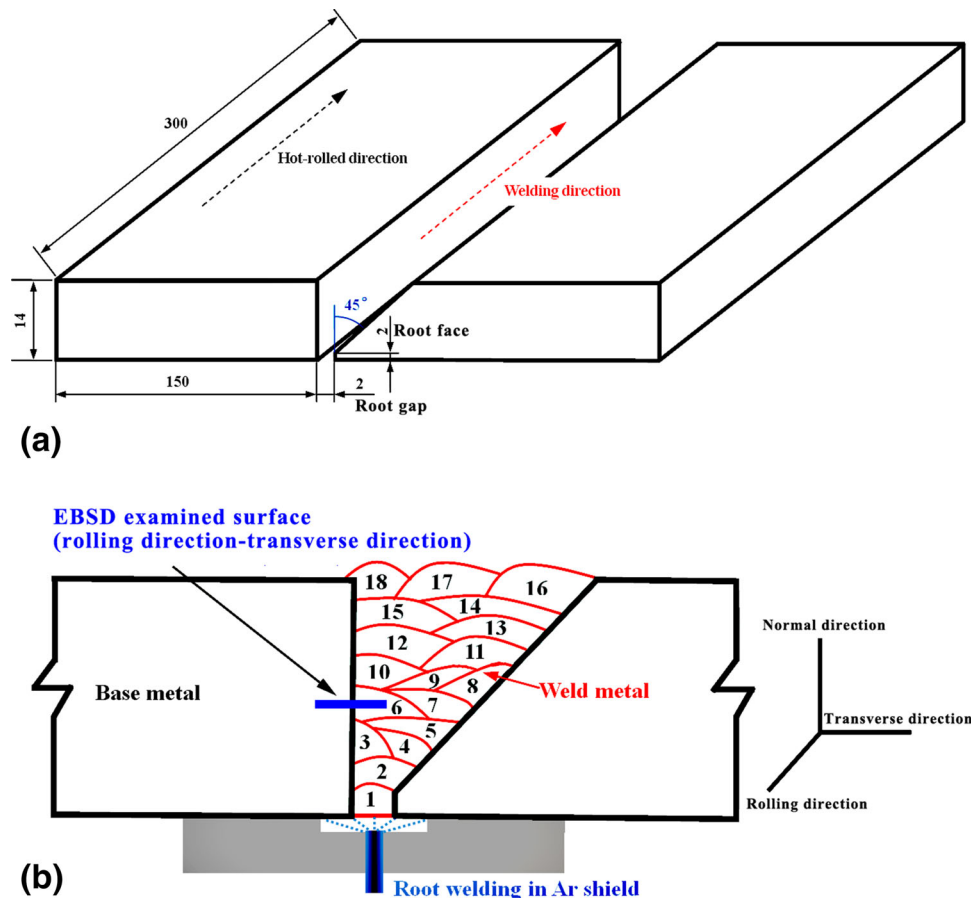


Fig. 1 Schematic diagrams of (a) welding process and (b) welding pass arrangement and EBSD examined surface

designed to study impact toughness of different zones in the DSS joint. This single bevel had a root gap of 2 mm and a root face of 2 mm without backing plate. The welding direction was paralleled to the rolling direction of the DSS plate. A total of 18 beads were needed for the 14-mm-thick DSS plate, as shown schematically in Fig. 1(b). The Ar purging gas at 20 L/min was applied in the process of root welding and maintained until the third pass was completed. In addition, the welding was performed in the pure Ar shielding gas at 20 L/min. The welding parameters are listed in Table 2. The heat input (Q , kJ/mm) was expressed as:

$$Q = \eta \frac{U * I}{S} \quad (\text{Eq 1})$$

where I welding current, U welding voltage, S welding speed, η welding thermal efficiency (0.61). The average heat input was 0.64 kJ/mm. The interpass temperature was controlled at < 150 °C.

The temperature field during the GTAW process was calculated by using SYSWELD software. According to actual beads by the OM observation, a 3-D finite element model including WM, HAZ, and BM was established. In the WM and its vicinity, a fine mesh has been considered. A double-ellipsoid heat source model was used for simulating heat source. The temperature-dependent physical properties of the BM and the WM such as density, specific heat, and thermal conductivity were obtained from previous reports (Ref 27-29). The heat inputs used in the simulation are listed in Table 2. Finally, the finite element simulation result was compared with the actual joint morphology to verify indirectly the accuracy of simulation. However, it is very necessary that temperature cycle curves are measured at different distances from the fusion line by using thermocouples and then compared with the simulation result. In the future, we will do a special study on welding temperature field and residual stress distribution in the DSS GTAW welding process.

2.2 Microstructure Characterization

To observe the microstructures of the WM, HAZ, and BM in the DSS welding joint, a cross-sectional sample was ground up to 2000 grit using series of SiC abrasive papers, polished with diamond paste in 0.5 μm diameter, and then electrolytically etched using 10 wt.% oxalic acid solution for 15-20 s at 0.4 A direct current, following which the microstructure was characterized by OM (ZEISS, Axio Vert.A1) and SEM (ZEISS, EVO 18) coupled with EDS (OXFORD, X-Max^N). The volumetric fractions of the austenite in the different regions were calculated by using the OM with Pro-Image software. To

Table 2 Welding parameters

Pass number	Current, A	Voltage, V	Welding speed, mm/s	Heat input, kJ/mm
1	104	11	0.67	1.11
2	132	12	2.60	0.40
3	132	12	3.38	0.30
4	132	12	2.75	0.37
5	132	13	1.48	0.75
6	132	13	1.53	0.73
7	132	13	2.10	0.53
8	148	14	3.05	0.44
9	147	13	2.42	0.51
10	148	13	2.36	0.53
11	148	13	2.00	0.63
12	148	13	2.63	0.48
13	148	13	1.37	0.91
14	150	13	1.59	0.80
15	150	13	1.42	0.89
16	121	12	1.61	0.59
17	121	12	1.62	0.58
18	121	12	1.85	0.51

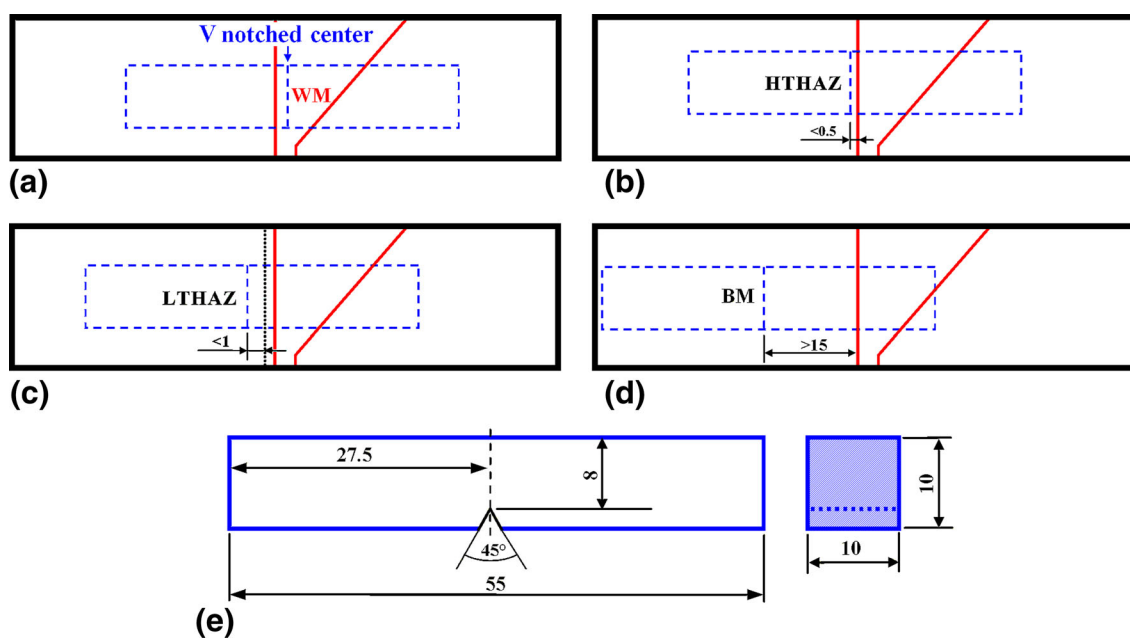
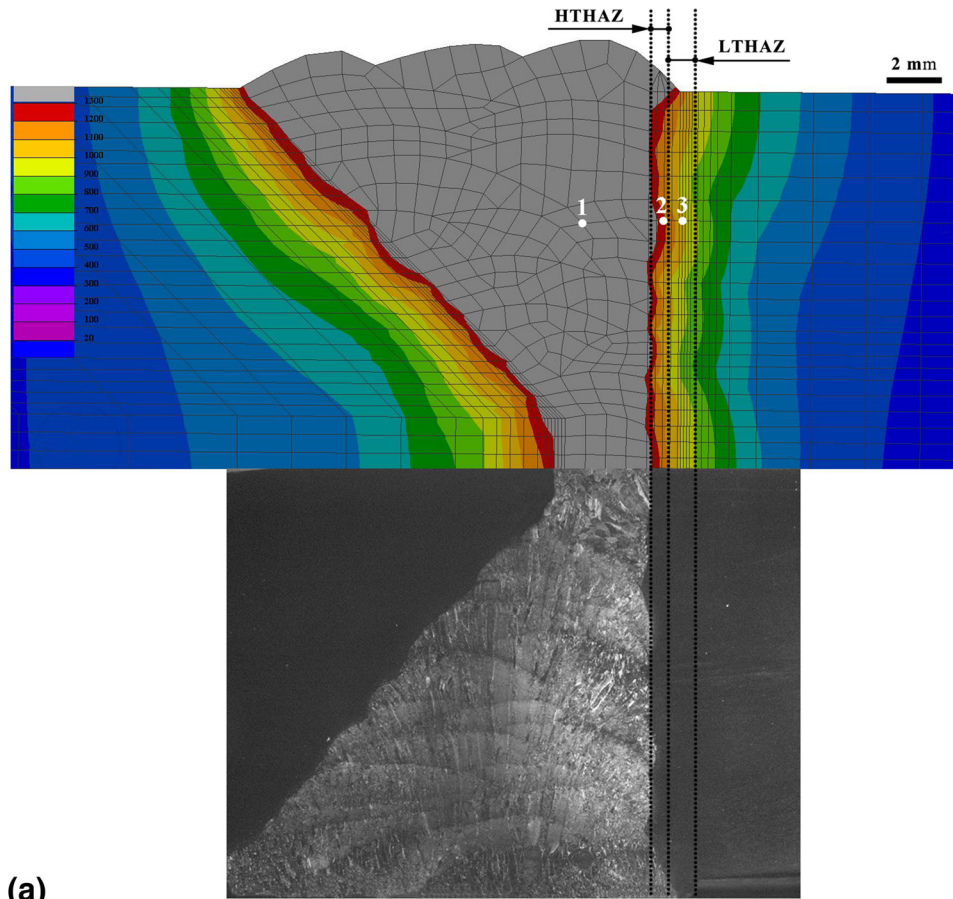
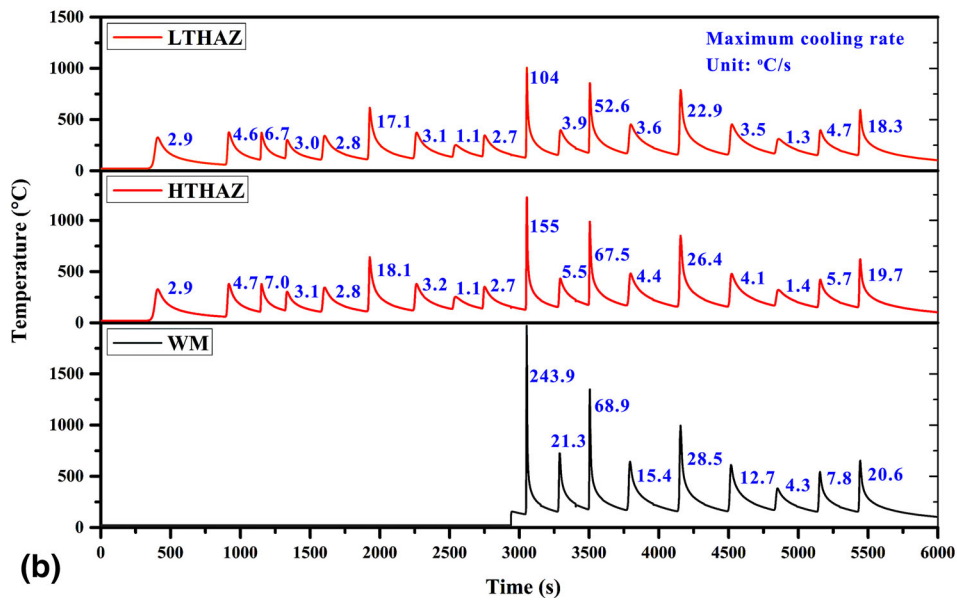


Fig. 2 Schematic diagrams of impact test at (a) WM, (b) HTHAZ, (c) LTHAZ, (d) BM, and (e) impact specimen size



(a)



(b)

Fig. 3 Welding thermal simulation and HAZ division: (a) cross-sectional macrostructure and temperature field (peak temperature) of the DSS welding joint; (b) temperature cycle curves and maximum cooling rates in the WM (node 1), HTHAZ (node 2), and LTHAZ (node 3)

obtain accurate results, at least ten OM images (according to ASTM E 562-11 (Ref 30) in each zone were collected at 500× magnification, and then these images were successively processed, including grayness transform, binarization, and phase extraction and calculation, and finally the average value was calculated. The OM coupled with the Pro-Image software provided a nice functional module to calculate phase content. In addition, the small precipitates were further characterized by TEM (FEI, Tecnal G2 F30).

The grain orientation analysis was performed by EBSD (OXFORD, NordlysMax²). After mechanical-polished to mirror-finish using the diamond paste with 0.25 μm diameter followed by electrolytic-polished with a 98 vol.% ethyl alcohol and 2 vol.% perchloric acid (HClO₄) solution applying 45 V at 20 °C for 20 s, a cross-sectional sample in rolling direction-transverse direction plane (see Fig. 1b) was prepared for EBSD analysis.

The chemical compositions of the different phases after electrochemically etching at 10 wt.% oxalic acid solution were measured by EPMA instrument (FE-EPMA, JXA-8530F). The quantitative calibrations of metallic elements (including Fe, Cr, Mo, Ni, Si, Mn, and Cu) and nitrogen were performed by using the corresponding high-pure metals and boron nitride, respectively. To reduce the random error, the least ten times measurements for each phase in the different zones were performed and then the average values were used as final results. In addition, a cross-sectional sample for EPMA mapping was prepared by same procedure as the EBSD analysis. The EPMA instrument contained five wavelength-dispersive spectrometers for mapping.

A commercial software FactSage equipped with FSstel database was used to calculate the nitrogen solubility in ferrite and austenite and evaluate which nitride was most likely to precipitate. In general, one nitride with the higher activity forms more possibly.

2.3 Impact Toughness Test

Impact toughness tests were performed in four typical zones: WM, high-temperature HAZ (HTHAZ), low-temperature HAZ (LTHAZ), and BM. The sampling schematics are shown in Fig. 2(a) to (d). The impact specimens were prepared with dimensions of 55 × 10 × 10 mm with 2 mm V notched at the

center (see Fig. 2e). Before the V-notch was processed, the specimen was slightly etched to ensure that the V-notch center was accurately located in the tested zones. Due to the narrower width of the HTHAZ (<0.5 mm) and the LTHAZ (<1 mm), a molybdenum wire with a 0.1 mm diameter was used to wire-cut the V-notch, and the HTHAZ V-notch center should be close to the fusion line. However, the impact fracture should be checked to ensure that the specimen was fractured in the tested zone, especially for the HTHAZ and the LTHAZ. Based on the SEM fracture examination, the effective impact test in the HTHAZ and the LTHAZ must meet the following conditions: (a) the initial position of impact fracture lies in the HTHAZ and the LTHAZ; and (b) the impact fracture area of the HTHAZ and the LTHAZ is more than 60% of the total fracture area. All the impact tests were carried out at -40 °C according to the ASTM: E23-16c standard (Ref 31). An automatic cooling device was used to cool the specimen to test temperature. The specimen was fractured immediately after being removed from the cooling container. The impact tests in each zone were performed in triplicate, and their average value was calculated as the test result.

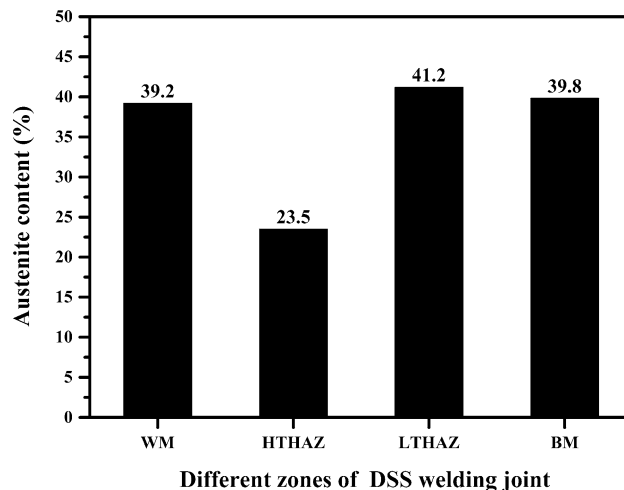


Fig. 5 Austenite contents of the different zones in the DSS welding joint

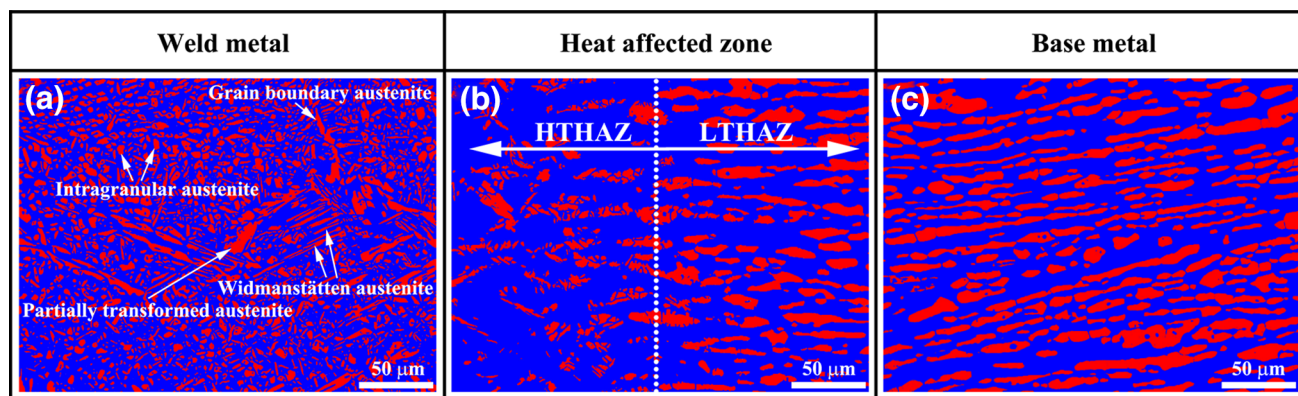


Fig. 4 Optical microstructures in the different zones of the DSS welding joint: (a) WM; (b) HTHAZ and LTHAZ; (c) BM

3. Results and Discussion

3.1 Microstructure Characterization

3.1.1 Temperature Field and OM Analysis. Figure 3(a) shows cross-sectional macrostructure and temperature field (peak temperature) of the DSS multi-pass welding joint. All 18 weld beads can be clearly observed and exhibited a perfect-fused state. The macrostructure is dominated by columnar primary ferrite grains which solidify first from liquid metal during cooling, and the growth of the ferrite columns is controlled by the temperature gradient, as reported by Comer (Ref 32). The gray in the WM showed the peak temperatures reached above 1300 °C which indicated the WM has melted completely. Undoubtedly, the peak temperature for each pass

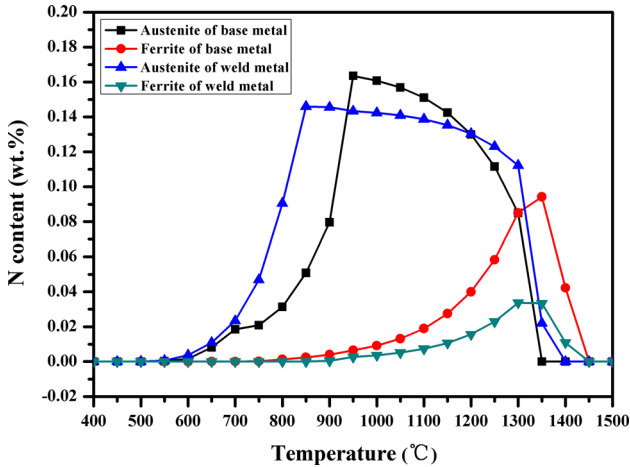


Fig. 6 Temperature-dependent nitrogen solubility in the ferrite and the austenite

during the multi-pass process was different. However, in order to visually distinguish WM, HTHAZ, and LTHAZ and compare clearly with the actual joint morphology to verify indirectly the accuracy of simulation, the maximum value of the temperature legend was set as 1300 °C in Fig. 3(a). Thus, all the passes in the WM shows same color. Generally, carbon steel HAZ can be divided into several subzones (including coarse-grained HAZ, fine-grained HAZ, and integrated HAZ) due to the different welding thermal cycles. However, since the narrower wide and unapparent grain changes as compared with carbon steel HAZ, the DSS HAZ can be divided into HTHAZ and LTHAZ. The peak temperature of the HTHAZ reached above 1100 °C, while the peak temperature of the LTHAZ is approximately in the range of 900-1100 °C, as reported by Jebaraj et al. (Ref 25, 33). When the reheating peak temperature was below 900 °C, there were not any changes in the microstructure of the DSS HAZ due to rapid cooling rate and short dwelling time at high temperature, as reported by Ramirez et al. (Ref 15). Figure 3(b) shows temperature cycle curves and maximum cooling rates in the WM, the HTHAZ, and the LTHAZ. In multi-pass welding process, the underlying and side WM as well as HAZ were reheated to above 900 °C by deposition of the adjacent beads and then rapidly cooled, while the reheating temperature from other far beads was below 900 °C. In addition, the cooling rate of the HTHAZ (maximum cooling rate when the pass closest to the HTHAZ was welded: 155 °C/s) was significantly higher than that of the LTHAZ (maximum cooling rate when the pass closest to the HTHAZ was welded: 104 °C/s), which may be a main reason for insufficient austenite formation in the HTHAZ as compared with the LTHAZ.

Figure 4(a), (b) and (c) shows optical microstructures of the WM, the HAZ, and the BM in the DSS welding joint. In the DSS welding joint, the austenite contains two types: primary austenite and γ_2 (Ref 15, 20, 21, 34). The primary austenite are directly solidified from residual liquids among the ferritic

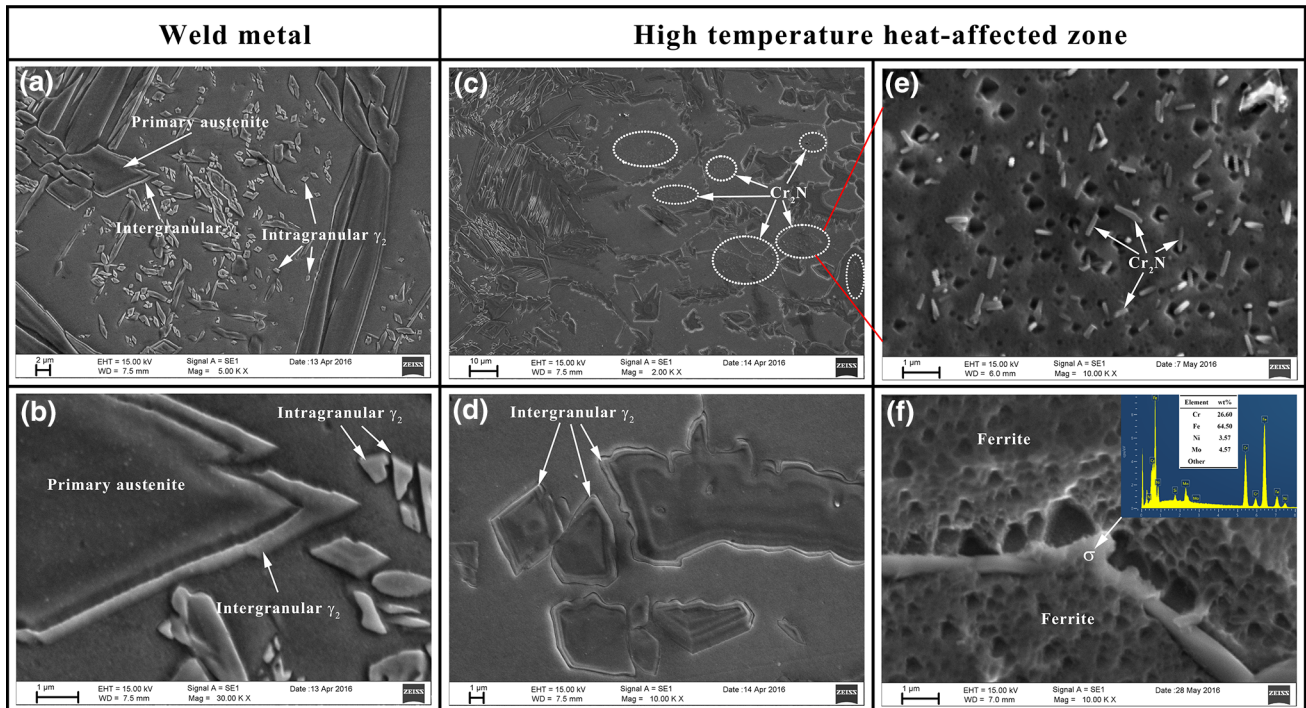


Fig. 7 Microstructure characterization by the SEM in (a) and (b) WM and (c)-(f) HTHAZ

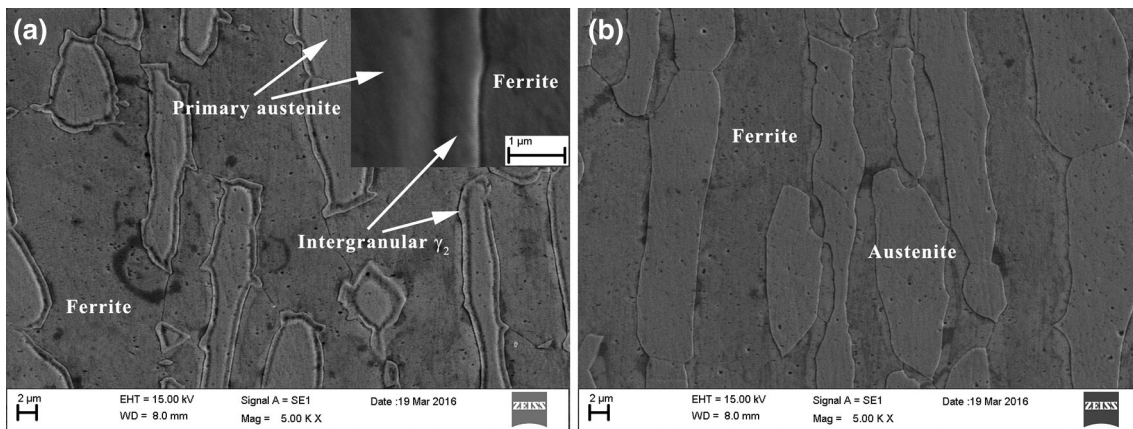


Fig. 8 Microstructure characterization by the SEM in (a) LTHAZ and (b) BM

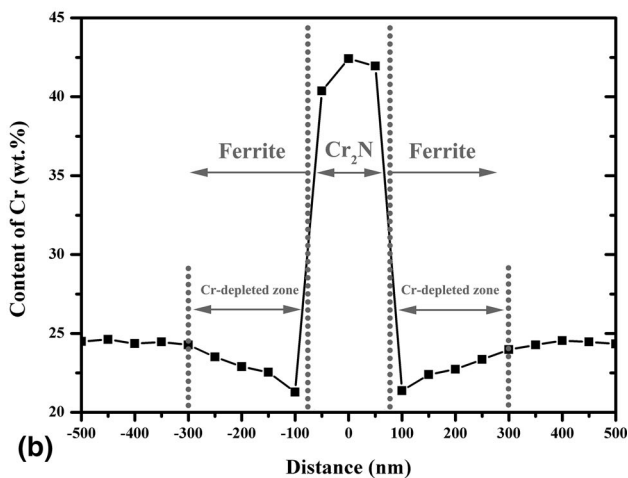
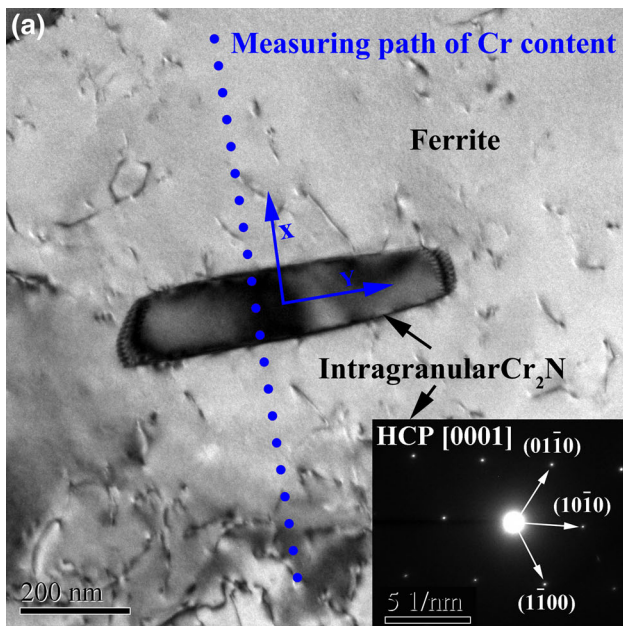


Fig. 9 Cr_2N characterization by the TEM: (a) the Cr_2N morphology and electron diffraction pattern; (b) the line analysis of Cr content along the Cr_2N

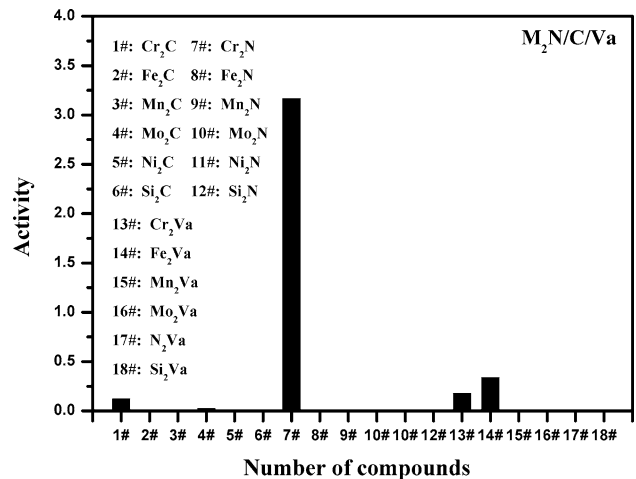


Fig. 10 Activities of different M_2N in the base material

dendrites as well as formed from the subsequent solid-state phase transition of the ferrite into the austenite. According to precipitation mechanism and morphology, the primary austenite is divided into grain boundary austenite, Widmanstätten austenite, intragranular austenite, and partially transformed austenite. The grain boundary austenite first begun to nucleate and grew at the prior ferrite boundaries (Ref 35, 36). When cooling continued and the available nucleation sites at the ferrite boundaries decreased and then if time permitted, the side-plate Widmanstätten austenite begun to nucleate and grew toward the ferrite side (Ref 36, 37). The intragranular austenite can form at the Ni-/N-rich regions within the ferrite grain. Since the intragranular austenite formation needs more undercooling as a driving force compared to the grain boundary austenite and the Widmanstätten austenite because of its higher activation energy for lattice diffusion, the intragranular austenite growth was limited, and thus resulted in finer grains (see Fig. 4a), as reported by Eghlimi et al. (Ref 35). In addition, a small amount of residual austenite was remained in the ferrite when reheating to ferritic temperature, named partially transformed austenite, which appeared as a plateau structure. The residual partially transformed austenite had important influence on preventing the ferrite growth effectively (Ref 35, 38). The HTHAZ

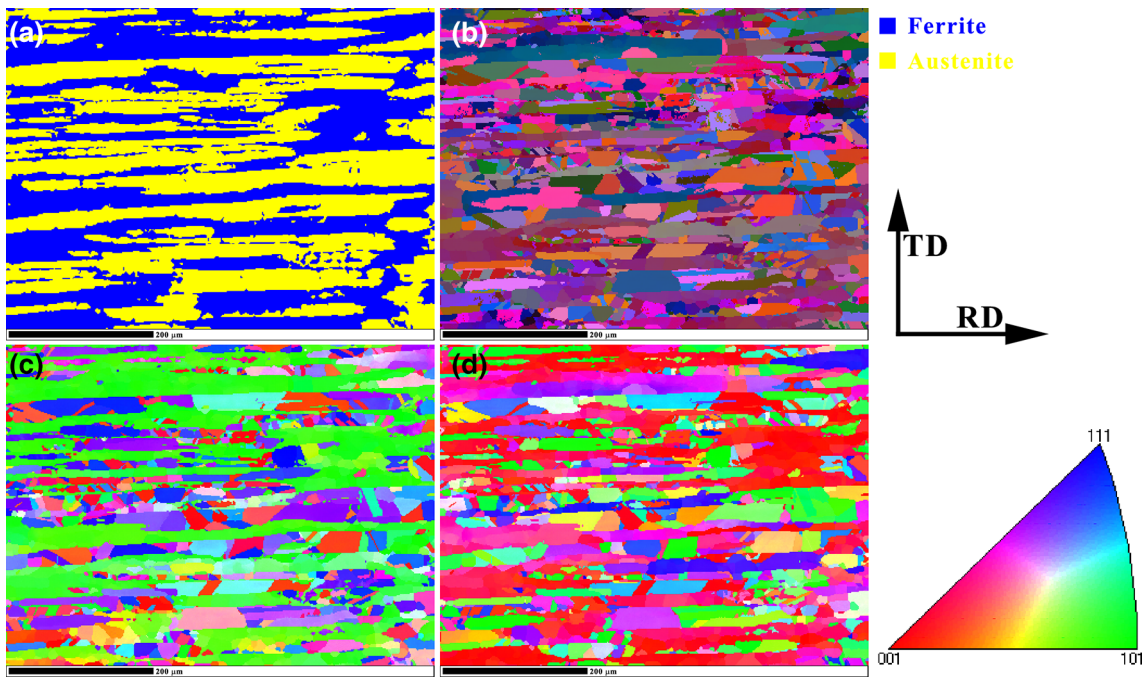


Fig. 11 EBSD images of the BM: (a) phase map presenting the ferrite in blue and the austenite in yellow; (b) Euler map showing the orientation of different ferrite and austenite grains; (c) IPF in the rolling direction; (d) IPF in the normal direction

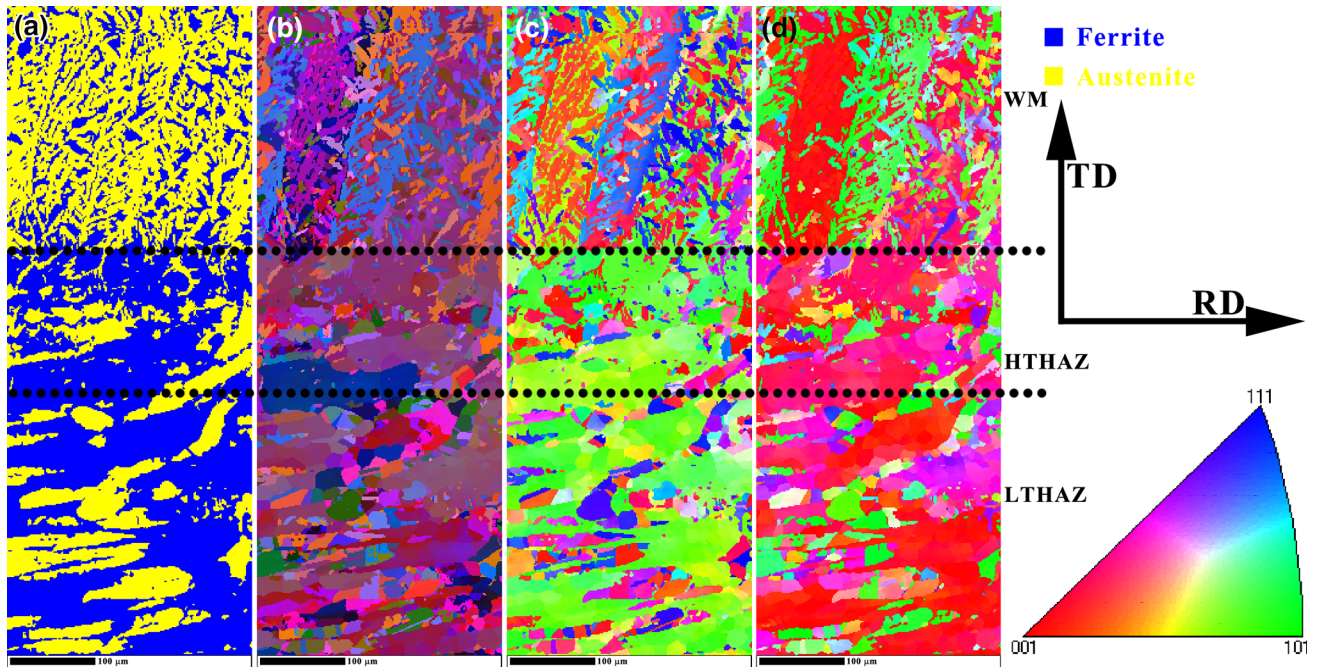


Fig. 12 EBSD images of the whole joint including the WM, HTHAZ, and LTHAZ: (a) phase map presenting the ferrite in blue and the austenite in yellow; (b) Euler map showing the orientation of different ferrite and austenite grains; (c) IPF in the rolling direction; (d) IPF in the normal direction

contained coarse ferrite grains with insufficient austenite content (Ref 15). However, the ferrite and austenite grains in the LTHAZ become fine and equiaxed due to partial dynamic recovery and recrystallization resulting from a combination of welding thermal cycle and slight welding strain. In combination

with temperature field (Fig. 3a), the microstructure observation (Fig. 4b) indicated that the HTHAZ wide was less than 0.5 mm while the LTHAZ wide reached about 1 mm.

The austenite contents of the different zones in the DSS welding joint are shown in Fig. 5. The HTHAZ presented the

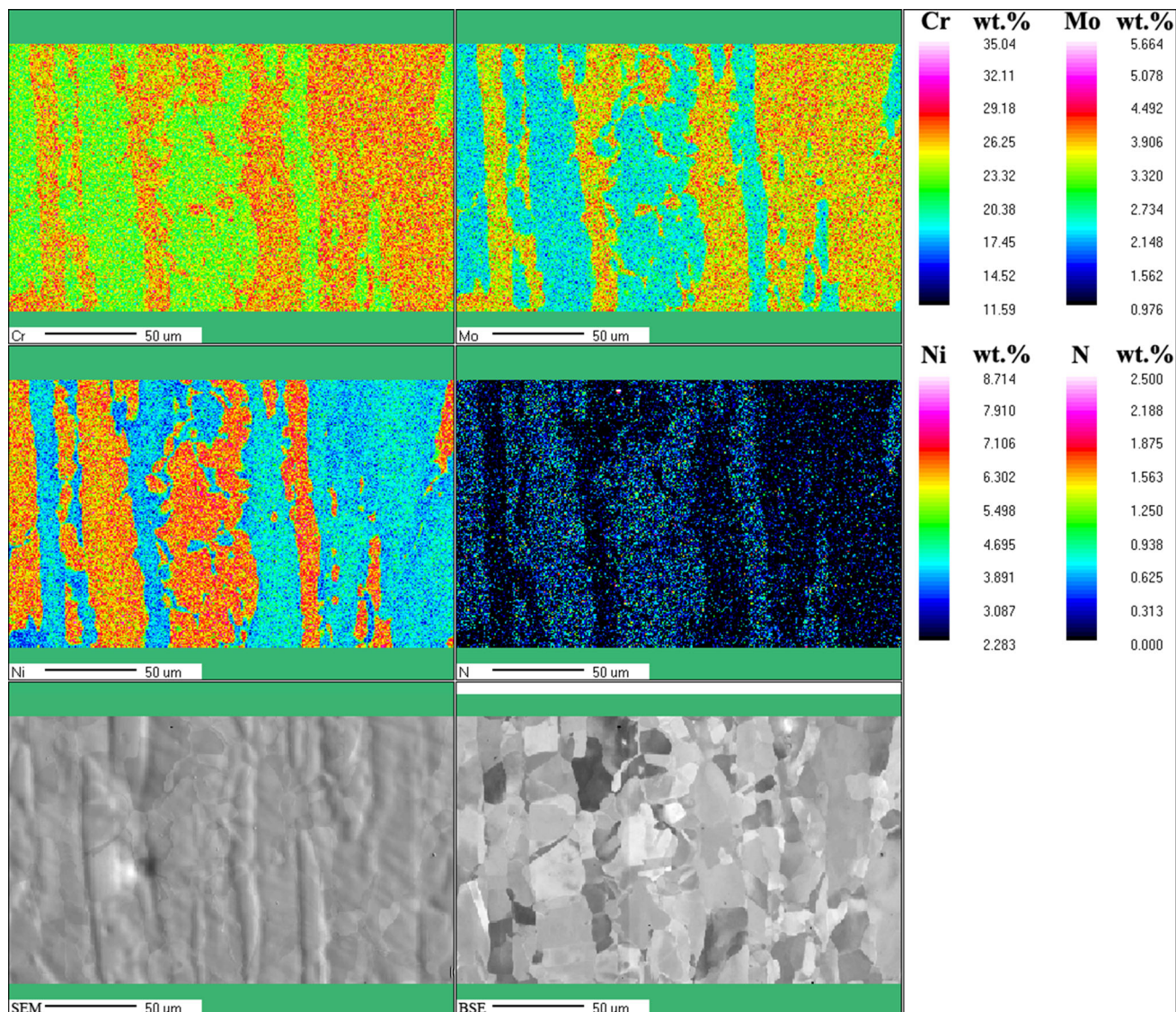


Fig. 13 Distribution of different elements in the BM

lowest austenite content (23.5%) as compared with the WM (39.2%), the LTHAZ (41.2%), and the BM (39.8%), which is due to higher peak temperature and more rapid cooling rate than the LTHAZ (see Fig. 3b) in addition to lower Ni and Cu contents than the WM (see Table 1). Generally, the ferrite phase belongs to brittle phase in comparison with the austenite phase (Ref 23, 39), and the excessive ferrite is one of the key factors to lead to relatively low toughness.

3.1.2 Secondary Phase. In the multi-pass welding, underlying and side WM as well as HAZ is reheated by depositions of the subsequent beads and then the apparent microstructural changes in these reheated zones are γ_2 and Cr_2N precipitation (Ref 15, 20). Under the solution annealed condition, the DSS retains almost all the nitrogen within the austenite because of high solubility and low diffusion of nitrogen in the austenite as compared to that in the ferrite, as reported by Westin and Ogawa et al. (Ref 40, 41). Figure 6 also reveals that this solubility difference at equilibrium state is very

large at relatively wide temperature range, as reported by Zhang et al. (Ref 17). Thus, as the partially ferritized microstructure cools rapidly from the elevated temperature, the ferrite, whether in the WM or the HAZ, would become supersaturated in nitrogen. When this metastable structure in the WM and the HAZ is reheated, the γ_2 and Cr_2N precipitation would compete with each other, as reported Ramirez et al. (Ref 15, 17). There are two different types of γ_2 observed in the WM and the HAZ, as shown in Fig. 7(a), (b), (d), and 8(a). The first type is the intragranular γ_2 , which nucleates and grows intragranularly in the ferrite. However, it is hard to distinguish the intragranular primary austenite and intragranular γ_2 . Generally, the intragranular γ_2 has smaller size than the intragranular primary austenite. The second type is the intergranular γ_2 , which forms at the ferrite and primary austenite boundary and grows toward the ferrite side. The etching technique formed a clear step when the intergranular γ_2 had grown from the primary austenite, which can be easily observed by the SEM. It can be clearly seen

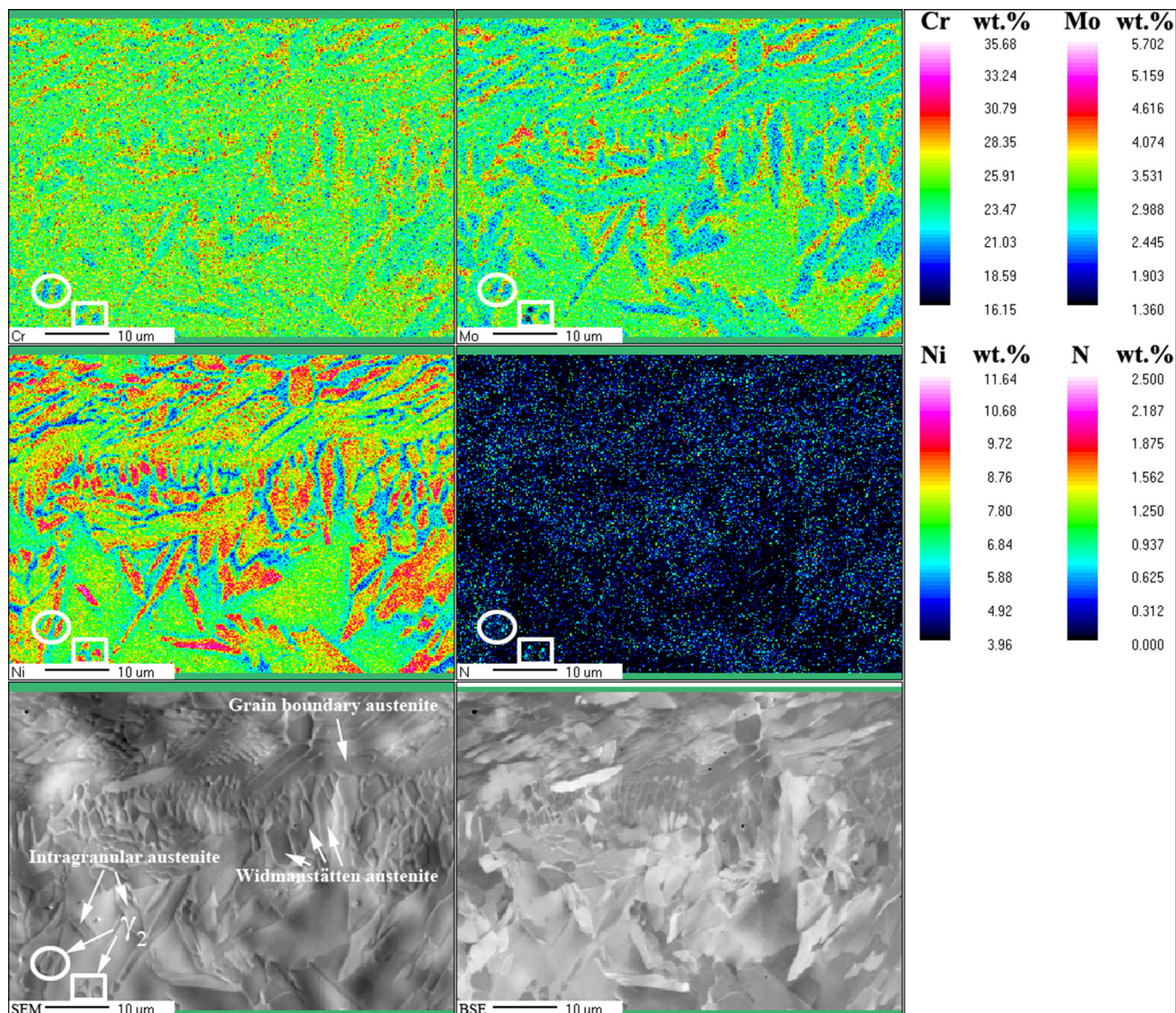


Fig. 14 Distribution of different elements in the WM

that the intergranular γ_2 formed in the LTHAZ (see Fig. 8a) which is another significant difference as compared with the BM except the grains in the LTHAZ tend to be equiaxed. The intergranular γ_2 precipitation in the LTHAZ could be one of the reasons why the LTHAZ had a slightly higher austenite content than the BM. Ramirez et al. (Ref 20) reported that the γ_2 were precipitated at reheating temperature above 900 °C, which was in agreement with the temperature field in combination with SEM observation in the HTHAZ and the LTHAZ.

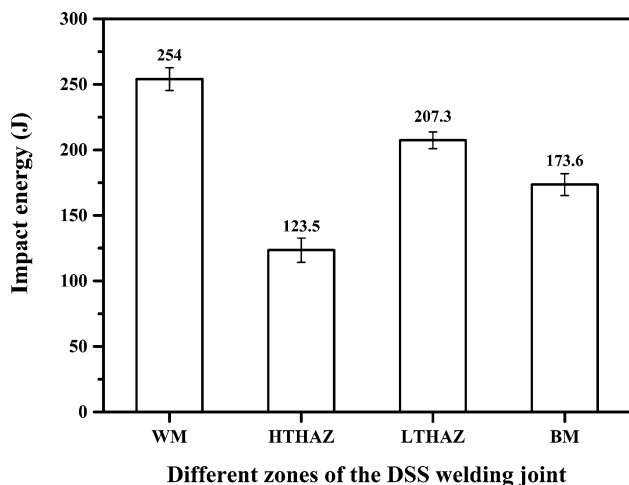
Furthermore, in the HTHAZ, the Cr_2N was prone to precipitation at the austenite-free ferrite regions (see Fig. 7c and e). The Cr_2N presented a rod-like morphology. Figure 9(a) reveals that the Cr_2N belongs to a closely packed hexagonal structure, as reported by Ramirez et al. (Ref 2, 15). The EDS analysis in the TEM shows that the rod-like Cr_2N mainly

enriched in Cr (41.58 wt%), N (6.81 wt%), and Mo (5.31 wt%). Based on thermodynamic analysis (see Fig. 10), the M_2N -type nitride with closely packed hexagonal structure is likely to be Cr_2N , which is in agreement with the EDS result. The EDS line analysis in the TEM (see Fig. 9b) indicates that the Cr enrichment in the Cr_2N resulted in the Cr-depleted zone formation in the ferrite adjacent to the Cr_2N , as reported by Kim et al. (Ref 2, 16). The previous studies reported that the Cr_2N can reduce the toughness and the corrosion resistance (Ref 1, 17, 19). However, the Cr_2N was not observed in the WM and the LTHAZ, which may be due to the reduction of the ferrite supersaturated in nitrogen. In addition, the σ phases were observed at the ferrite/ferrite boundary in the HTHAZ, as shown in Fig. 7(f). The EDS analysis shows that the σ phase enriched in more Cr and Mo elements than the ferrite, as

Table 3 Chemical compositions of different phases in the different zones

Zone	Phase	Element (wt.%)			
		Cr	Mo	Ni	N
WM	Ferrite	23.768	3.048	7.967	0.043
	Grain boundary austenite	22.963	2.781	8.443	0.293
	Widmanstätten austenite	22.535	2.663	9.219	0.234
	Intragranular austenite	22.351	2.635	9.318	0.120
	Partially transformed austenite	23.481	2.979	7.977	0.198
HTHAZ	Secondary austenite	22.026	2.477	9.818	0.079
	Ferrite	24.497	3.829	4.544	0.039
	Primary austenite	23.314	3.294	6.247	0.352
	Secondary austenite	22.004	2.572	6.916	0.200
	Cr ₂ N	41.58	5.31	...	6.81
LTHAZ	Sigma	27.58	5.48	2.87	...
	Ferrite	23.996	3.832	4.592	0.042
	Primary austenite	22.162	2.532	6.407	0.263
	Secondary austenite	21.624	2.492	6.894	0.202
BM	Ferrite	24.401	3.852	4.441	0.045
	Austenite	21.633	2.511	6.765	0.257

Chemical compositions of the ferrite and the austenite were measured by the EPMA
Chemical composition of the Cr₂N was analyzed by the EDS attached in the TEM
Chemical composition of the σ phase was analyzed by the EDS attached in the SEM

**Fig. 15** Impact energy of the different zones in the DSS welding joint

reported by Nria et al. (Ref 18, 42, 43). In general, the nucleation of the σ phase at the ferrite grain boundaries is easier than in the bulk because the reduction of grain boundary free energy favors σ precipitation. The same as the Cr₂N, the brittle σ phase can reduce the toughness of DSS (Ref 17).

3.1.3 Orientation Analysis Based on EBSD. Figure 11 and 12 show EBSD images of the BM and the whole joint (WM + HTHAZ + LTHAZ), respectively. The BM presented a typical banded structure of alternating austenite and ferrite grains elongated in the rolling direction (Ref 44). The Euler map (see Fig. 11b) revealed that the austenite grains were fragmented indicating a partial or complete recrystallization process after solution treatment, but the unapparent recrystal-

lization occurred in the ferrite grains. The inverse pole figures (IPF) of the BM in the rolling direction (see Fig. 11c) and in the normal direction (see Fig. 11d) showed that most of the ferrite grains in the BM presented a typical rolling texture component $\{001\}\langle 110\rangle$, while the austenite grains showed random orientation, as reported by Badji et al. (Ref 44). The Euler map in the LTHAZ reveals that the banded ferrite and austenite grains became equiaxed, while the coarse ferrite grains and fine austenite grains were observed in the HTHAZ, as shown in Fig. 12(b). However, the ferrite grains both in the HTHAZ and in the LTHAZ maintained the same texture as the banded ferrite in the BM, as shown in Fig. 12(c) and (d). In the HTHAZ, the fine intragranular austenite grains were mainly randomly oriented, whereas the coarse primary austenite grains were close to Kurdjumov-Sachs (KS) orientation relationship, as reported by Karlsson et al. (Ref 45). In the WM, the columnar ferrite has one single orientation throughout a grain, whereas several families of austenite appeared. However, the ferrite texture disappeared in the WM. In the future, the recrystallized degree, special boundary, misorientation, and texture in the different zones of the DSS welding joint will be further studied based on the EBSD.

3.1.4 Element Distribution. Figure 13 and 14 show the element distribution in the BM and WM, respectively. The chemical compositions of the different phases in the different zones are listed in Table 3. Whether in the BM, the WM or the HAZ, the ferrite stabilizers such as Cr and Mo were enriched in the ferrite, while the austenite stabilizers such as Ni and nitrogen were concentrated in the austenite (Ref 2). However, the partitioning of metallic elements in the WM, especially for low-nitrogen DSS, is not as apparent as in the BM, as reported by Westin et al. (Ref 40, 41). Westin et al. (Ref 40) have studied the element partitioning by EPMA mapping LDX 2101 DSS

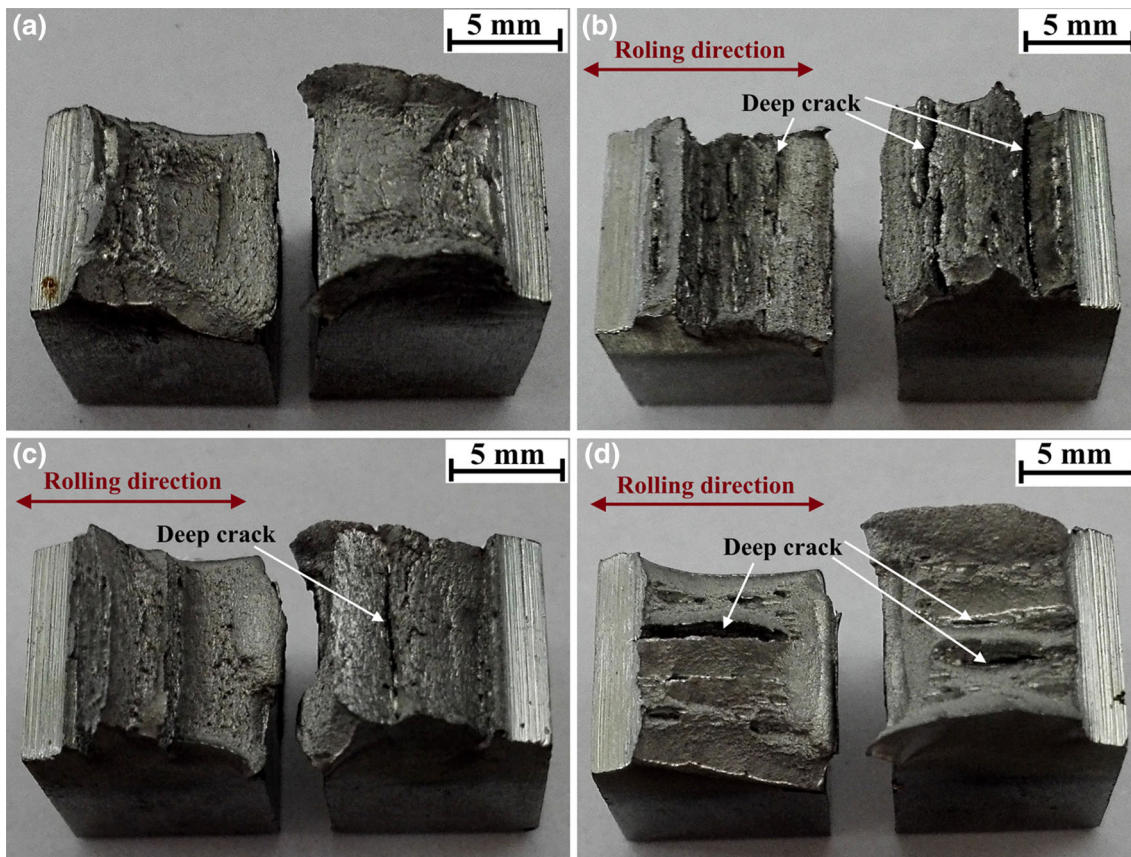


Fig. 16 Macrofracture surfaces: (a) WM; (b) HTHAZ; (c) LTHAZ; (d) BM

weld and revealed that segregation of metallic elements could follow the dendritic solidification structure. Ogawa et al. (Ref 41) drew a conclusion that nitrogen alloying can promote the partitioning of the Ni and nitrogen in the austenite, while the Cr and Mo in the ferrite. In the WM, the Widmanstätten austenite has lower amounts of Cr, Mo, and nitrogen than the grain boundary austenite, although enriched in Ni, because it forms at lower temperatures and after consumption of most of the alloying elements by the grain boundary austenite, as reported by Eghlimi et al. (Ref 2, 35). The intragranular austenite exhibited slightly lower Cr and Mo contents and higher Ni content than other primary austenite. In addition, the γ_2 in each zone had higher Ni content but significantly lower Cr and Mo contents than the primary austenite, as reported by Ramirez et al. (Ref 2, 4, 15, 34). However, the same as the primary austenite, the γ_2 enriched in the nitrogen as compared with the ferrite.

3.2 Impact Toughness

3.2.1 Impact Energy of Different Zones. Figure 15 shows impact energy of the different zones in the DSS welding joint. The WM exhibited the highest impact toughness (impact

energy 254 J). The HTHAZ had the lowest impact toughness (impact energy 123.5 J). It is surprised to note that the impact energy of the LTHAZ reached 207.3 J which was obviously higher than the HTHAZ (123.5 J) and the BM (173.6 J).

3.2.2 Impact Fracture Analysis. Figure 16(a), (b), (c) and (d) shows macrofracture surfaces of the WM, HTHAZ, LTHAZ, and BM, respectively. As an indication of good toughness, the WM macrofracture presented an even surface without wide and deep cracks. The HTHAZ macrofracture surface had many deep cracks, and some cracks grew even through entire macrofracture, which indicated relatively low toughness. In addition, the LTHAZ macrofracture presented a few cracks with smaller depth and width than the BM and the HTHAZ macrofracture, which indicated a higher toughness in the LTHAZ.

Figure 17(a), (b), (c) and (d) presents microfracture surfaces of the WM. The austenite dimple fracture was main fracture mode, and the dimple sizes presented a wide range from 0.2 to 15 μm resulted from different sizes and types of austenite. In general, the dimples of intragranular primary austenite and γ_2 were smaller than other primary austenite, as shown in Fig. 18. The fine γ_2 can effectively prevent crack growth through the

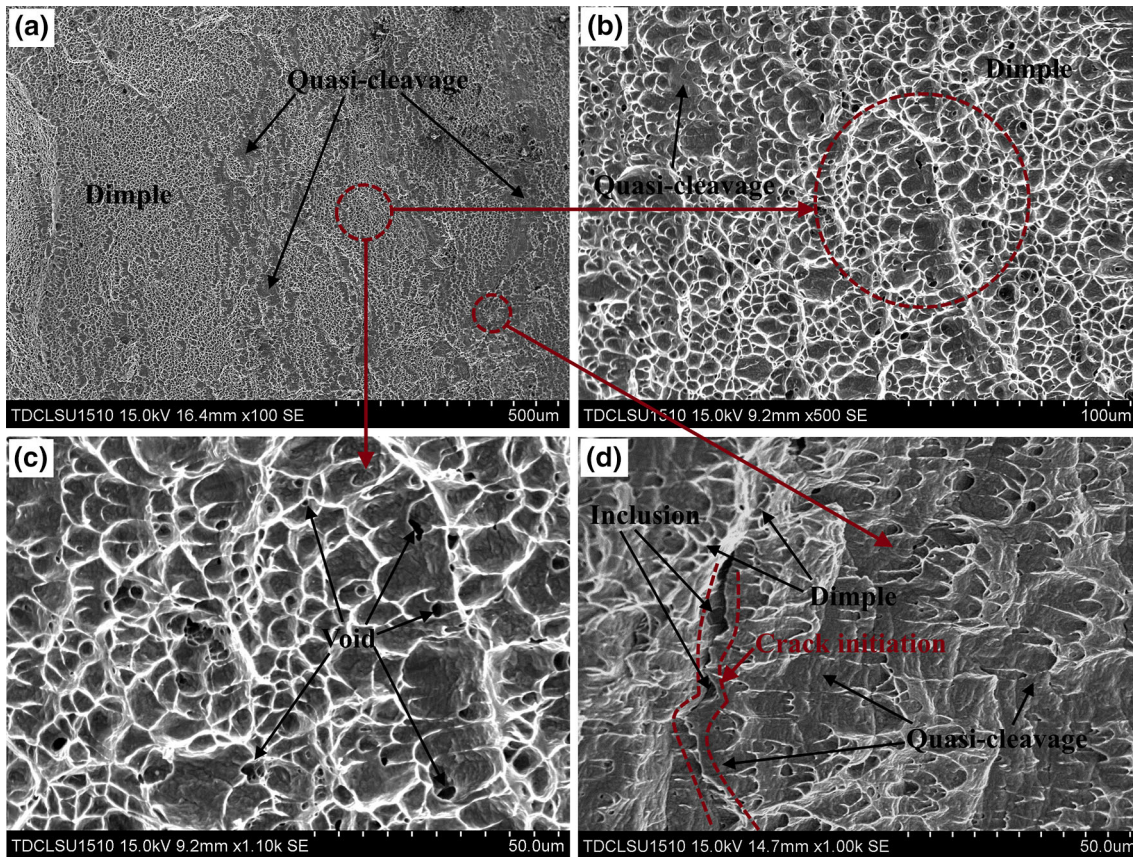


Fig. 17 Microfracture surfaces of the WM: (a) low-magnification observation at $\times 100$; (b)-(d) high-magnification observation at $\times 500$ and $\times 1000$

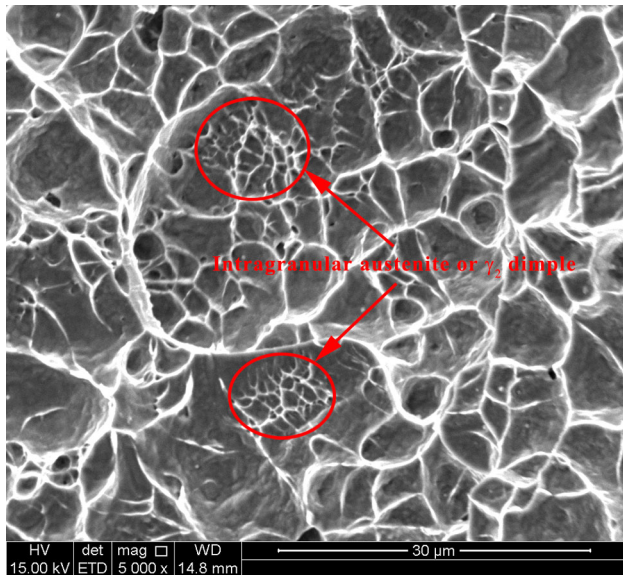


Fig. 18 Dimples of fine intragranular primary austenite or secondary austenite in the WM

brittle ferrite grain by absorbing more impact energy than the primary austenite, as reported by Zhang et al. (Ref 15, 17). The ferrite microfracture exhibited a mixed mode of dimple and

quasi-cleavage, which exhibited small cleavage facets and many tearing ridges. Furthermore, there were many voids in the microfracture, which may be resulted from the inclusions. The WM had excellent impact toughness, which may be because of (a) sufficient ductile austenite formation (Fig. 4a, 5, and 12a); (b) the dense austenite grains with different orientations in the ferrite matrix (Fig. 12b, c and d); and (c) unapparent ferrite texture (Fig. 12b, c and d).

Figure 19(a), (b), (c) and (d) shows microfracture surfaces of the HTHAZ. The fracture mode of the HTHAZ is dominated by the ferrite cleavage fracture. The cleavage fracture showed a flat fracture surface and shallow tearing ridge. The crack grew through the coarse ferrite grain resulting in rapid cleavage fracture. However, the grain boundary austenite can prevent the spread of the crack, as shown in Fig. 19(c). Figure 19(d) reveals the fine austenite such that the γ_2 and intragranular primary austenite can retard crack growth. In addition, there were also many voids found in the ferrite fracture surface, which could be originated from inclusions and secondary precipitates (Ref 24). The σ and nitride precipitation could promote the brittle fracture in the HTHAZ, as shown in Fig. 20. However, the fine γ_2 can effectively prevent the growth of the crack. In a word, the HTHAZ had relatively low impact toughness, which was because of (a) coarse ferrite grain and insufficient austenite formation; (b) hard and brittle σ and Cr_2N precipitation resulting in stress concentration; and (c) obvious ferrite texture.

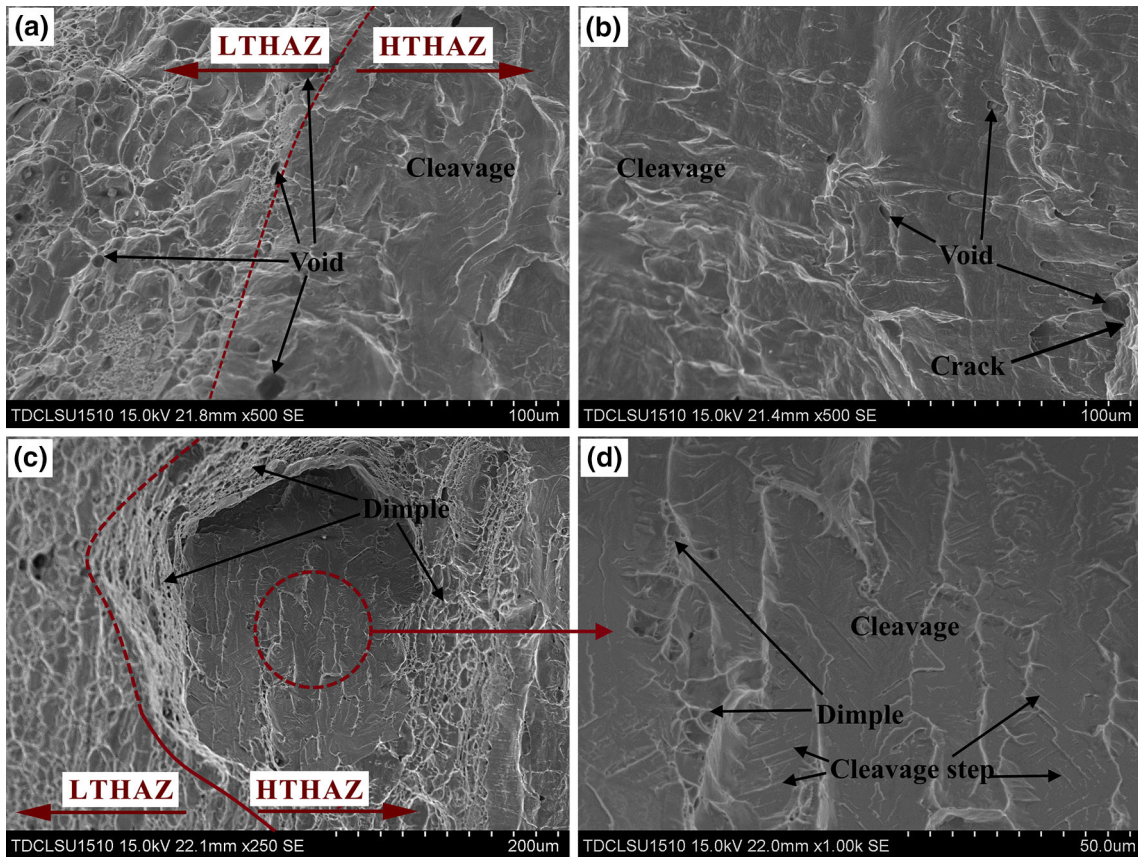


Fig. 19 Microfracture surfaces of the HTHAZ: (a) and (b) the cleavage fracture with a flat fracture surface and shallow tearing ridge; (c) crack growth through the coarse ferrite grain; (d) ductile austenite retarding crack growth

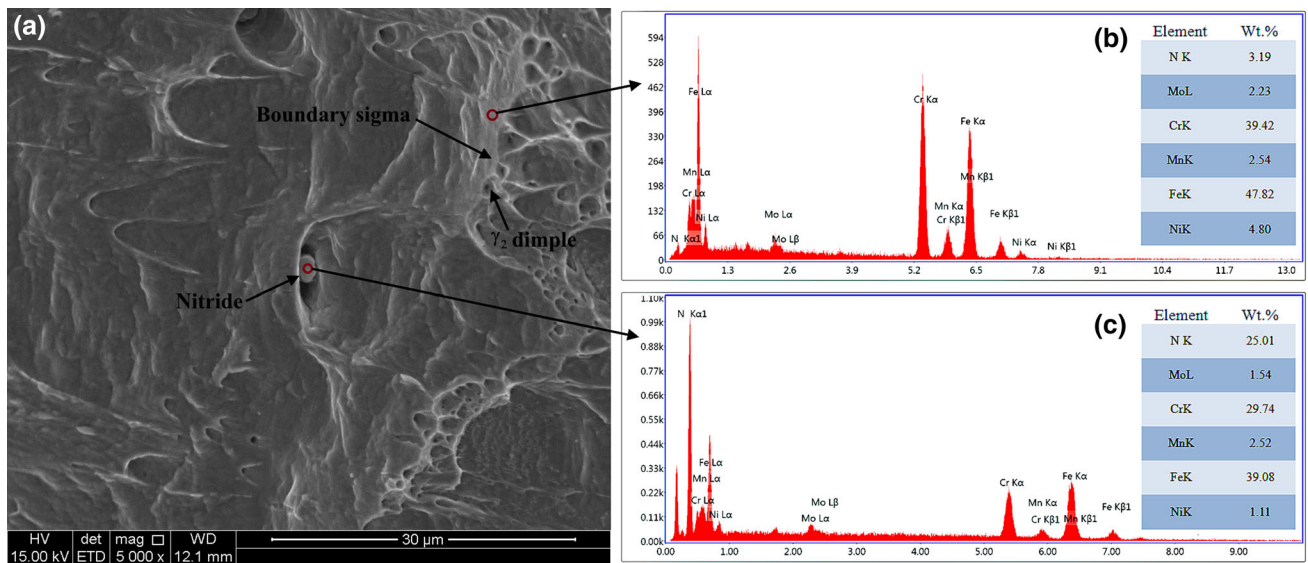


Fig. 20 Characterizations of sigma and nitride in the HTHAZ: (a) SEM image; (b) EDS analysis of sigma; (c) EDS analysis of nitride

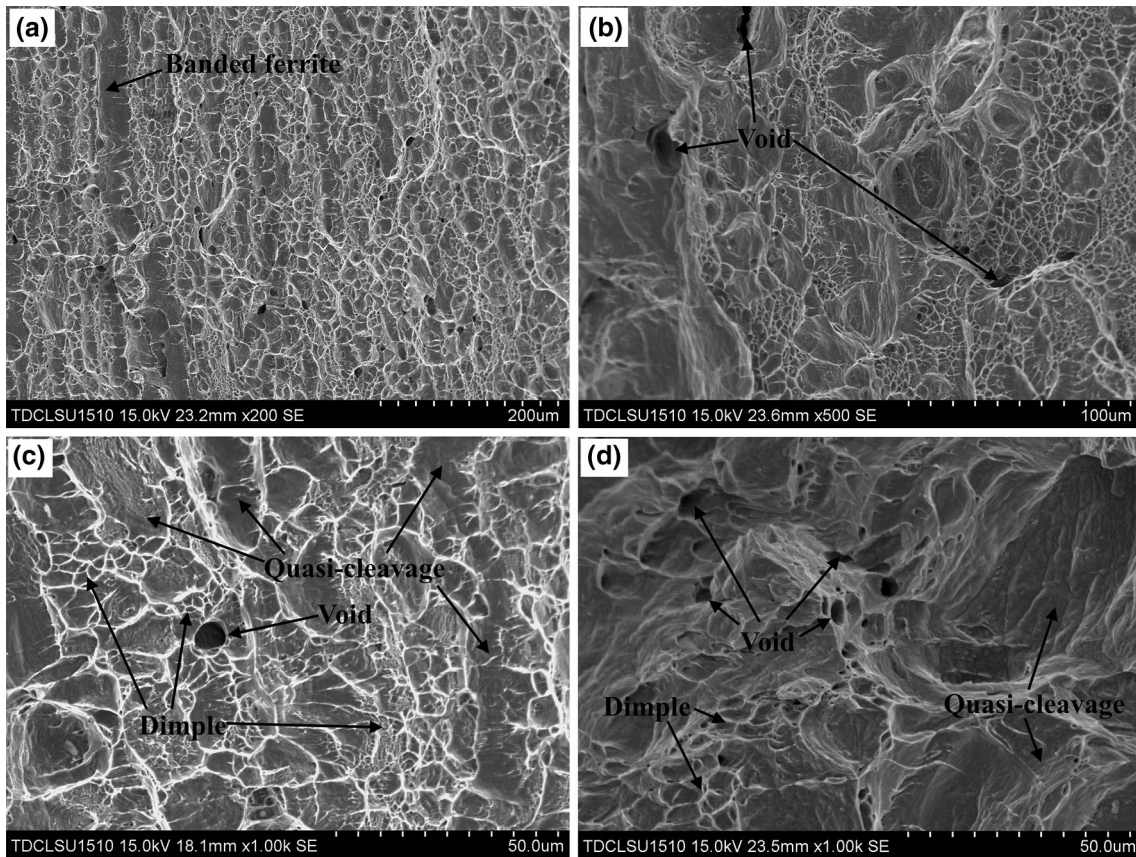


Fig. 21 Microfracture surfaces of the LTHAZ: (a) low-magnification observation at $\times 200$; (b)–(d) high-magnification observation at $\times 500$ and $\times 1000$

Figure 21(a), (b), (c) and (d) shows microfracture surfaces of the LTHAZ. The LTHAZ exhibited a mixed fracture mode of austenite dimple fracture and ferrite quasi-cleavage fracture. The austenite dimples had a wide size range from 0.2 to 10 μm . There were many small dimples within the large dimple. In addition, the ferrite quasi-cleavage fracture was surrounded by large amounts of intricate dimples. The intergranular γ_2 precipitation in the primary austenite and ferrite boundary may be one main reason that the LTHAZ had higher toughness than the BM. In addition, the elongated grains experienced the partial recovery and recrystallization process and transformed into equiaxed grains due to the welding heat cycles, which may be another reason for the LTHAZ with higher toughness.

Figure 22(a), (b), (c) and (d) shows microfracture surfaces of the BM. Similarly to the LTHAZ, the BM also exhibited a mixed fracture mode with dimples and quasi-cleavage facets. However, there were some evident differences in fracture characteristics between the BM and the LTHAZ: (a) the BM fracture presented alternating bands resulting from elongated ferrite and austenite grains and (b) the ferrite quasi-cleavage fracture in the BM showed deeper tearing ridge and more apparent ductile characteristics like big dimples. The irregular inclusions could cause the discontinuous fracture of the material resulting in the void formation, as presented in Fig. 22(b) and (d). However, the small spherical inclusions can promote the dimple formation, as shown in Fig. 22(c).

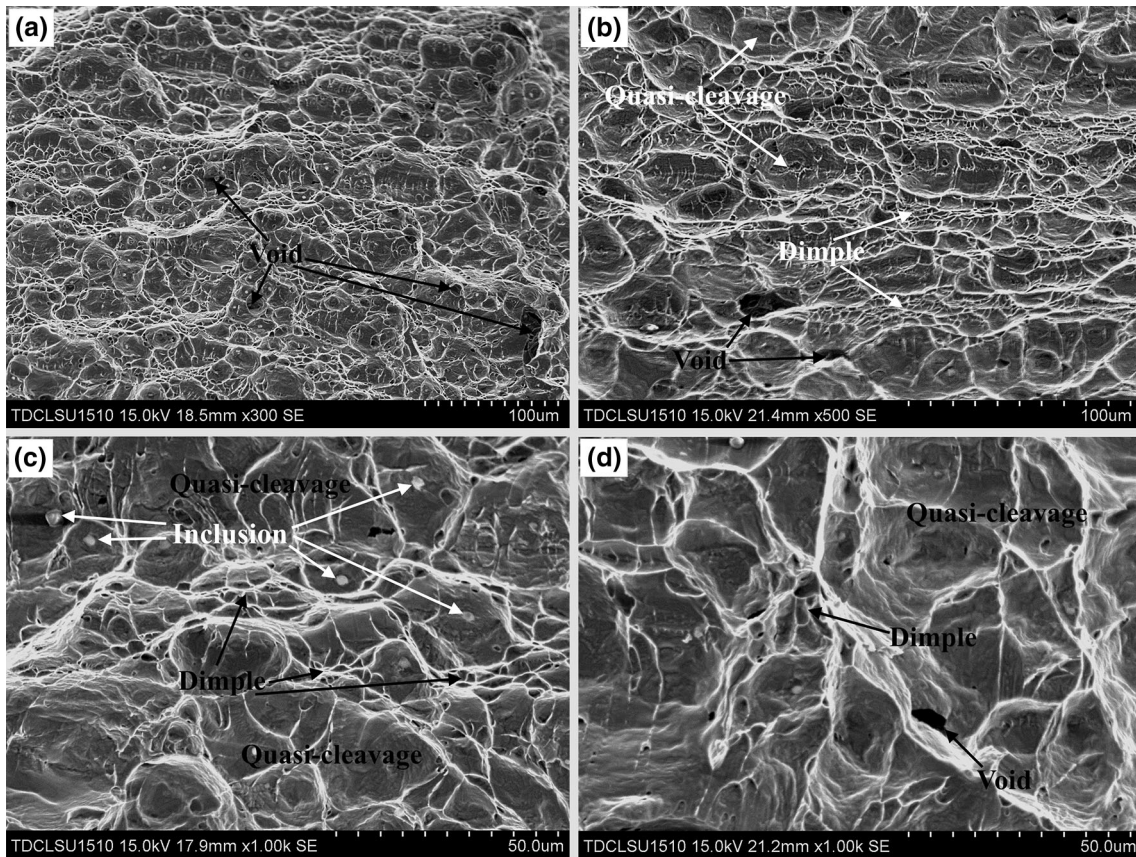


Fig. 22 Microfracture surfaces of the BM: (a) low-magnification observation at $\times 300$; (b)–(d) high-magnification observation at $\times 500$ and $\times 1000$

4. Conclusions

1. Based on microstructural characterization and temperature field analysis, the DSS GTAW HAZ can be divided into HTHAZ and LTHAZ. The HTHAZ contained coarse ferrite grains with insufficient austenite and secondary precipitates such as the γ_2 , Cr_2N , and σ phase. In the LTHAZ, the most apparent change in microstructure was intergranular γ_2 precipitation. In the WM and HTHAZ, the austenite consisted of different primary austenite and secondary austenite.
2. Most of the ferrite grains in the BM presented a typical rolling texture component $\{001\}\langle 110\rangle$, while the austenite grains showed random orientation. Both in the HTHAZ and in the LTHAZ, the ferrite grains maintained the same texture as the banded ferrite in the BM. In the WM, the columnar ferrite has one single orientation throughout a grain, whereas several families of austenite appeared. However, the ferrite texture disappeared in the WM.
3. The austenite in the BM and the WM enriched in Ni and nitrogen, while Cr and Mo were concentrated in the ferrite, and thus, no element showed clear dendritic distribution in the WM. The γ_2 had higher Ni content but significantly lower Cr and Mo content than the primary austenite. However, the same as the primary austenite, the nitrogen was enriched in the γ_2 as compared to the ferrite.
4. The WM exhibited the highest impact toughness, which was because of sufficient ductile austenite formation, the

dense austenite grains with different orientations, and unapparent ferrite texture; the HTHAZ had the lowest impact toughness, which was because of coarse ferrite grain, insufficient austenite formation, hard and brittle σ and Cr_2N precipitation, and obvious ferrite texture; the impact energy of the LTHAZ reached 207.3 J which was obviously higher than the HTHAZ and BM due to the intergranular γ_2 precipitation.

5. The WM fracture mode was dominated by the austenite dimple fracture. The ferrite cleavage fracture was main fracture mode in the HTHAZ. The BM and the LTHAZ exhibited a mixed fracture mode of austenite dimple fracture and ferrite quasi-cleavage fracture.

Acknowledgment

This work was supported by the National Natural Science Foundation of China [Grant Number 51575382] and Marine Economic Innovation and Development of Regional Demonstration Projects of China [Grant number cxsf2014-12].

References

1. J.C. de Lacerda, L.C. Cândido, and L.B. Godefroid, Effect of Volume Fraction of Phases and Precipitates on the Mechanical Behavior of UNS S31803 Duplex Stainless Steel, *Int. J. Fatigue*, 2015, **74**, p 81–87

2. Z.Q. Zhang, H.Y. Jing, L.Y. Xu, Y.D. Han, L. Zhao, and J.L. Zhang, Influence of Microstructure and Elemental Partitioning on Pitting Corrosion Resistance of Duplex Stainless Steel Welding Joints, *Appl. Surf. Sci.*, 2017, **394**, p 297–314
3. F. Mirakhorli, F.M. Ghaini, and M.J. Torkamany, Development of Weld Metal Microstructures in Pulsed Laser Welding of Duplex Stainless Steel, *J. Mater. Eng. Perform.*, 2012, **21**, p 2173–2176
4. J.O. Nilsson, L. Karlsson, and J.O. Andersson, Secondary Austenite Formation and Its Relation to Pitting Corrosion in Duplex Stainless Steel Weld Metal, *Mater. Sci. Tech.*, 1995, **11**, p 276–283
5. W.T. Tsai and M.S. Chen, Stress Corrosion Cracking Behavior of 2205 Duplex Stainless Steel in Concentrated NaCl Solution, *Corros. Sci.*, 2000, **42**, p 545–559
6. F. Zanotto, V. Grassi, A. Balbo, C. Monticelli, and F. Zucchi, Stress Corrosion Cracking of LDX 2101[®] Duplex Stainless Steel in Chloride Solutions in the Presence of Thiosulphate, *Corros. Sci.*, 2014, **80**, p 205–212
7. A.A. El-Yazgi and D. Hardie, Stress Corrosion Cracking of Duplex and Super Duplex Stainless Steels in Sour Environments, *Corros. Sci.*, 1998, **40**, p 829–898
8. Petroleum and Natural Gas Industries-Materials for Use in H₂S-Containing Environments in Oil and Gas Production-Part 3: Cracking-Resistant CRAs (Corrosion-Resistant Alloys) and Other Alloys, 15156-3, ISO, 2003, p. 31–32
9. D.H. Kang and H.W. Lee, Study of the Correlation Between Pitting Corrosion and the Component Ratio of the Dual Phase in Duplex Stainless Steel Welds, *Corros. Sci.*, 2013, **74**, p 396–407
10. Y.J. Guo, T.Y. Sun, J.C. Hu, Y.M. Jiang, L.Z. Jiang, and J. Li, Microstructure Evolution and Pitting Corrosion Resistance of the Gleeble-Simulated Heat-Affected Zone of a Newly Developed Lean Duplex Stainless Steel 2002, *J. Alloy. Compd.*, 2016, **658**, p 1031–1040
11. R.B. Bhatt, H.S. Kamat, S.K. Ghosal, and P.K. De, Influence of Nitrogen in the Shielding Gas on Corrosion Resistance of Duplex Stainless Steel Welds, *J. Mater. Eng. Perform.*, 1999, **8**, p 591–597
12. K.D. Ramkumar, D. Mishra, B. Ganesh Raj, M.K. Vignesh, G. Thiruvengatam, S.P. Sudharshan, N. Arivazhagan, N. Sivashanmugam, and A.M. Rabel, Effect of Optimal Weld Parameters in the Microstructure and Mechanical Properties of Autogeneous Gas Tungsten Arc Weldments of Super-Duplex Stainless Steel UNS S32750, *Mater. Des.*, 2015, **66**, p 356–365
13. L. Karlsson, Welding Duplex Stainless Steels-A Review of Current Recommendations, *Weld. World*, 2012, **56**, p 65–76
14. L. Karlsson, Welding Duplex and Super Duplex Stainless Steels, *Anti-Corros. Method. Mater.*, 1995, **42**, p 30–35
15. A.J. Ramirez, J.C. Lippold, and S.D. Brandi, The Relationship between Chromium Nitride and Secondary Austenite Precipitation in Duplex Stainless Steels, *Metall. Mater. Trans. A*, 2003, **34**, p 1575–1597
16. H. Kim, S. Jeon, S. Kim, I. Lee, Y. Park, K. Kim, and Y. Kim, Investigation of the Sensitization and Intergranular Corrosion of Tube-to-Tubesheet Welds of Hyper Duplex Stainless Steel Using an Electrochemical Reactivation Method, *Corros. Sci.*, 2014, **87**, p 60–70
17. Z.Q. Zhang, H.Y. Jing, L.Y. Xu, Y.D. Han, and L. Zhao, Investigation on Microstructure Evolution and Properties of Duplex Stainless Steel Joint Multi-Pass Welded by Using Different Methods, *Mater. Des.*, 2016, **109**, p 670–685
18. R. Badji, M. Bouabdallah, B. Bacroix, C. Kahloun, B. Belkessa, and H. Maza, Phase Transformation and Mechanical Behavior in Annealed 2205 Duplex Stainless Steel Welds, *Mater. Charact.*, 2008, **59**, p 447–453
19. S. Kim, S. Jang, I. Lee, and Y. Park, Effects of Solution Heat-Treatment and Nitrogen in Shielding Gas on the Resistance to Pitting Corrosion of Hyper Duplex Stainless Steel Welds, *Corros. Sci.*, 2011, **53**, p 1939–1947
20. A.J. Ramirez, S.D. Brandi, and J.C. Lippold, Secondary Austenite and Chromium Nitride Precipitation in Simulated Heat Affected Zones of Duplex Stainless Steels, *Sci. Technol. Weld. Join.*, 2004, **9**, p 301–313
21. V. Muthupandi, P.B. Srinivasan, S.K. Seshadri, and S. Sundaresan, Effect of Nitrogen Addition on Formation of Secondary Austenite in Duplex Stainless Steel Weld Metals and Resultant Properties, *Sci. Technol. Weld. Join.*, 2004, **9**, p 47–52
22. T. Chehuan, V. Dreilich, K.S. de Assis, F.V.V. de Sousa, and O.R. Mattos, Influence of Multipass Pulsed Gas Metal Arc Welding on Corrosion Behaviour of A Duplex Stainless Steel, *Corros. Sci.*, 2014, **86**, p 268–274
23. M. Asif, K.A. Shrikrishna, P. Sathiya, and S. Goel, The Impact of Heat Input on the Strength, Toughness, Microhardness, Microstructure and Corrosion Aspects of Friction Welded Duplex Stainless Steel Joints, *J. Manuf. Process.*, 2015, **18**, p 92–106
24. K.D. Ramkumar, G. Thiruvengatam, S.P. Sudharshan, D. Mishra, N. Arivazhagan, and R. Sridhar, Characterization of Weld Strength and Impact Toughness in the Multi-Pass Welding of Super-Duplex Stainless Steel UNS 32750, *Mater. Des.*, 2014, **60**, p 125–135
25. A.V. Jebaraj and L. Ajaykumar, Influence of Microstructural Changes on Impact Toughness of Weldment and Base Metal of Duplex Stainless Steel AISI, 2205 for Low Temperature Applications, *Proc. Eng.*, 2013, **64**, p 456–466
26. S. Wessman, Evaluation of the WRC 1992 Diagram Using Computational Thermodynamics, *Weld. World*, 2013, **57**, p 305–313
27. X.J. Jin, L.X. Huo, Y.F. Zhang, B.R. Bai, X.W. Li, and J. Cao, Finite Element Analysis of Modeling Residual Stress Distribution in All-Position Duplex Stainless Steel Welded Pipe, *J. Mater. Sci. Technol.*, 2004, **20**, p 387–390
28. J. Chen and B. Young, Stress-Strain Curves for Stainless Steel at Elevated Temperatures, *Eng. Struct.*, 2006, **28**, p 229–239
29. C. Lee and K. Chang, Comparative Study on Girth Weld-Induced Residual Stresses between Austenitic and Duplex Stainless Steel Pipe Welds, *Appl. Therm. Eng.*, 2014, **63**, p 140–150
30. Standard Test Method for Determining Volume Fraction by Systematic Manual Point Count, E562-11, ASTM, 2011, p. 1–7
31. Standard Test Methods for Notched Bar Impact Testing of Metallic Materials, E23-16c, ASTM, 2012, p. 1–27
32. A. Comer, Corrosion Fatigue of a Superduplex Stainless Steel Weldment. Ph.D. Thesis, Dublin City University, 2003
33. E.M. Westin, Microstructure and Properties of Welds in the Lean Duplex Stainless Steel LDX 2101. Ph.D. Thesis, Royal Institute of Technology, 2010
34. C.M. Garzón and A.J. Ramirez, Growth Kinetics of Secondary Austenite in the Welding Microstructure of A UNS S32304 Duplex Stainless Steel, *Acta Mater.*, 2006, **54**, p 3321–3331
35. A. Eghlimi, M. Shamanian, and K. Raeissi, Effect of Current Type on Microstructure and Corrosion Resistance of Super Duplex Stainless Steel Claddings Produced by the Gas Tungsten Arc Welding Process, *Surf. Coat. Technol.*, 2014, **244**, p 45–51
36. A. Eghlimi, M. Shamanian, M. Eskandarian, A. Zabolian, and J.A. Szpunar, Characterization of Microstructure and Texture Across Dissimilar Super Duplex/Austenitic Stainless Steel Weldment Joint by Super Duplex Filler Metal, *Mater. Charact.*, 2015, **106**, p 27–35
37. A. Eghlimi, M. Shamanian, M. Eskandarian, A. Zabolian, M. Nezakat, and J.A. Szpunar, Evaluation of Microstructure and Texture Across the Welded Interface of Super Duplex Stainless Steel and High Strength Low Alloy Steel, *Surf. Coat. Technol.*, 2015, **264**, p 150–162
38. Y.H. Yang, B. Yan, J. Li, and J. Wang, The Effect of Large Heat Input on the Microstructure and Corrosion Behaviour of Simulated Heat Affected Zone in 2205 Duplex Stainless Steel, *Corros. Sci.*, 2011, **53**, p 3756–3763
39. K. Yildizli, Investigation on the Microstructure and Toughness Properties of Austenitic and Duplex Stainless Steels Weldments under Cryogenic Conditions, *Mater. Des.*, 2015, **77**, p 83–94
40. E.M. Westin and S. Hertzman, Element Distribution in Lean Duplex Stainless Steel Welds, *Weld. World*, 2014, **58**, p 143–160
41. T. Ogawa and T. Koseki, Effect of Composition Profiles on Metallurgy and Corrosion Behavior of Duplex Stainless Steel Weld Metals, *Weld. Res. Suppl.*, 1989, **1**, p 181–191
42. S.M. Yang, Y.C. Chen, C.H. Chen, W.P. Huang, and D.Y. Lin, Microstructural Characterization of $\delta/\sigma/\gamma_2/\chi$ Phases in Silver-Doped 2205 Duplex Stainless Steel under 800 °C Aging, *J. Alloy. Compd.*, 2015, **633**, p 48–53
43. N.L. Isern, H.L. Luque, I.L. Jiménez, and M.V. Biezma, Identification of Sigma and Chi Phases in Duplex Stainless Steels, *Mater. Charact.*, 2016, **112**, p 20–29
44. R. Badji, B. Bacroix, and M. Bouabdallah, Texture, Microstructure and Anisotropic Properties in Annealed 2205 Duplex Stainless Steel Welds, *Mater. Charact.*, 2011, **62**, p 833–843
45. L. Karlsson and J.B. Rjesson, Orientation Relationships of Intragranular Austenite in Duplex Stainless Steel Weld Metals, *Sci. Technol. Weld. Join.*, 2014, **19**, p 318–323